Experimental demonstration of thermophones in vibro-acoustic noise cancellation scenario for varying gaseous media

Boris Leizeronok , Alex Kleiman , Shimon Julius , Avshalom Manela , Beni Cukurel *

Aerospace Engineering Faculty, Technion-IIT, Haifa, 3200003, Israel

ABSTRACT

The paper focuses on an analytical and experimental study of global noise cancellation between two co-planar thermo- and vibro-acoustic sources in varying gaseous media. To address the experimental uncertainty in thermophone thermal boundary condition, the previously developed theoretical model is expanded to consider oscillating temperature at the solid-fluid interface, beyond the previously studied oscillating heat flux boundary. The results of the analysis indicate that at the point of optimal cancellation, the ratio of acoustic sources' powers correlates to the specific heat ratio γ of the surrounding media through $\gamma/(\gamma-1)$ relation. Then, a thermophone device is designed using commonly available materials and is deposited on a conventional vibro-acoustic loudspeaker, which acts as the noise source. Both acoustic sources are placed in a sealed acoustic chamber and are experimentally studied in several fluid media with different specific heat ratio values (argon, nitrogen, carbon dioxide and norflurane). The constructive and destructive interferences of the two emitters are analyzed at an exemplary frequency for varying phase differences, and global noise cancellation is demonstrated in all gases using microphone measurements in different spatial locations. The empirical results are observed to fully agree with the theoretical predictions.

1. Introduction

Pressure field stimulation and sound production via Joule heating have been studied since the late 19th century. They were first noticed by Braun in a bolometer, where passage of an alternating current through a thin wire was observed to result in sound generation [1]. The term "thermophone" was coined by De Lange two decades later, to define an acoustic transmitter capable of producing sound through high frequency thermal oscillations [2]. These devices behave as electrical resistors, where an alternating electrical current is converted to produce surface thermal fluctuations and, consequently, pressure waves in the surrounding fluid, absent of mechanical motion [3]. Owing to their design simplicity, such transducers can offer a number of potential advantages over conventional vibro-acoustic devices, such as lightweight and robust static structure, capability of surface-wide emission, acoustic purity, and broad frequency range [4,5].

Although the thermo-acoustic effect in solids remained largely unexplored after its initial discovery due to limitations of available materials, at the turn of the 21st century thermophones regained the scientific community's interest with a seminal paper that described the construction of aluminum film ultrasound generators held midair by porous silicon [6]. In contrast to the early thermophone designs, which were constructed from simple thin metal wires and were already shown to have more efficient acoustic

* Corresponding author.
  E-mail address: beni@cukurel.org (B. Cukurel).

Nomenclature

Variables	Meaning (Units)
A	surface area (m^2)
CV	coefficient of variance (unitless)
E	energy per unit area (J m^{-2})
MW	molar mass of gas (kg mol)
Pr	Prandtl number (unitless)
PW	power (W)
Q	heat flux (W m^{-2})
$\mathscr{R}$	specific gas constant (J kg K^{-1})
RA_{avg}	average ratio (unitless)
Re	Reynolds number (unitless)
T	temperature (K)
U, u	velocity (m s^{-1})
U_y	uncertainty of calculated quantity (unitless)
a	acceleration (m s^{-2})
c	speed of sound (m s^{-1})
c_p	specific heat capacity at constant pressure (J kg K^{-1})
c_v	specific heat capacity at constant volume (J kg K^{-1})
e	thermal effusivity (W $s^{0.5}$ m^{-2} K^{-1})
f, g	general functions (unitless)
i	imaginary root of $\sqrt{-1}$ (unitless)
k	heat conduction coefficient (W m^{-1} K^{-1})
p	pressure (Pa)
t	time (s)
t_f	integration time (s)
x	spatial coordinate (m)
γ	heat capacity ratio unitless
ε	infinitesimal parameter unitless
η	efficiency (unitless)
μ_0	dynamic viscosity (Pa s)
ρ	density (kg m^{-3})
φ	phase (rad)
ω	angular frequency (rad s^{-1})

Acronyms meaning

Ar	argon
AIN	aluminum nitride
CO_2	carbon dioxide
FFT	Fast Fourier Transform
N_2	nitrogen
R134a	norflurane
RMS	root mean square
SPL	sound pressure level
SPR	sources' powers ratio

Subscripts and superscripts meaning

e	electric source
f	fluid
k	kinetic source
opt	optimal value
q	thermal source
sub	substrate
w	wall
0	nominal value
*	dimensional quantities

generation with decreasing heat capacity per unit volume [4], this device introduced thermally and electrically insulated backing. The impact of the additional layer on the electro-thermo-acoustic energy conversion process was examined experimentally using several similarly structured thermo-acoustic emitters (thin heated films over substrate material) and it was shown that the applied substrate also plays a significant role in sound production [7]. Consequently, advanced designs (such as suspended arrays of aluminum wires, carbon nanotubes, and graphene) were developed to explore the efficiency and performance envelopes of heat flux sound sources [5, 8–11]. Moreover, significant efforts have been invested to characterize the behavior of thermophones in different gaseous and liquid media [12–15]. Yet, the actual mechanism of converting the supplied electrical power into acoustic waveform in various gaseous media is not well-explored and there is an ambiguity in the literature regarding the amplitude of the acoustic pressure generated by thermophone devices and its dependency on the media properties [5,16–18].

During the past decade, thermo-acoustic transducers were also suggested to have practical application in the field of active noise cancellation. Noise reduction via active sound cancellation is a trending mechanism for diminishing acoustic pollution in a multitude of sectors (aviation, energy, transportation, military etc.) [19]. The basic concept relies on local annihilation of an unwanted pressure field through the creation of an out-of-phase sound wave at the same amplitude and frequency. Commonly termed "active noise cancellation", this approach relies on emitters, which are actively modulated by sensing elements in a control circuit. This typically involves an array of loudspeakers, which convert electric power into acoustic energy through vibro-mechanics. However, the geometric limitations of conventional loudspeakers prevent these anti-phase pressure emitters from being effectively used in a distributed manner. Therefore, the common implementation of noise cancellation is localized to the observer, rather than holistic elimination at the source.

In recent works, a theoretical model for the tonal noise cancellation of a vibrational source by a heat flux emitter has been suggested [20,21]. In this model, the linearized one-dimensional Navier-Stokes-Fourier equations have been applied to produce a set of mass, momentum and energy balances for the calculation of density, velocity, and temperature perturbations. Imposing time-sinusoidal variation of both normal velocity and normal heat-flux wall conditions, optimal sound reduction was obtained in cases where the signals had a common frequency and were generated out of phase. The optimal ratio between thermal and kinetic energies supplied at the boundary was found to depend on the particular fluid properties. Although prior experimental effort has demonstrated the feasibility of active vibro-acoustic noise cancellation in air [22], its dependency on the acoustic medium remained unvalidated. Moreover, due to the unclear nature of thermophone's thermal boundary condition in experimental studies, the theoretical formulation should be expanded to also consider oscillating temperature boundary and its impact on mutual cancellation of sources.

While still having numerous critical gaps, the concept of heat flux driven active noise cancellation can be considered a disruptive technology. With a static and surface-distributed sound emitter, the undesirable acoustic fields can be annihilated directly at the source boundaries, holding promise for truly silent bodies. Building upon the existing knowledge in the interaction of surface heat with sound emanating from a boundary, and heat driven acoustic field generation in solid media, present effort is devoted to expansion of the analytical framework to also cover temperature boundary conditions, as well as to experimental validation of active cancellation dependency on the fluid properties. Thereby, the work is intended to bridge the gaps in scientific and engineering knowledge towards feasible thermoacoustic noise cancellation in solid-gas interfaces.

Along these lines, a thermophone is designed using commonly available materials and deposited on a conventional vibro-acoustic loudspeaker, which acts as the unwanted noise source. Both the thermal transducer and the loudspeaker are placed in a sealed acoustic chamber and are experimentally characterized in several fluid media. The constructive and destructive interferences of the two emitters are presented at an exemplary frequency for varying phase differences and global noise cancellation is demonstrated using microphone measurements in different measurement locations. Finally, the empirical results are correlated with the theoretical predictions. According to the authors' knowledge, this is the first effort in scientific literature that not only demonstrates the feasibility of heat flux driven noise cancellation, but also experimentally studies its properties.

2. Theoretical model

Consider a semi-infinite expanse of a perfect gas confined by an infinite planar surface located at $x^* = 0$ (hereafter, asterisks denote dimensional quantities). The gas is nominally in thermodynamic equilibrium with the surface, with uniform density ρ_0^* and temperature T_0^*, with the latter equals to the nominal surface temperature. The boundary is harmonically actuated in the normal $\hat{x}$ direction into the gas layer, according to the prescribed velocity profile

$$U_w^*(t^*) = \varepsilon c_0^* \cos(\omega^* t^*)\hat{x}, \tag{1}$$

where $c_0^* = \sqrt{\gamma \mathscr{R}^* T_0^*}$ denotes the mean speed of sound in the gas, with γ and $\mathscr{R}^*$ marking the ratio of specific heats and the specific gas constant, respectively. In Eq. (1), $\varepsilon \ll 1$, so that the system description may be linearized about its nominal equilibrium. Adding to the vibroacoustic excitation, small-amplitude normal heat-flux or temperature oscillations are applied at the wall,

$$Q_w^*(t^*) = \varepsilon Q_\varepsilon^* \cos(\omega^* t^* + \varphi)\hat{x} \text{ or } T_w^*(t^*) = \varepsilon T_\varepsilon^* \cos(\omega^* t^* + \varphi)\hat{x}, \tag{2}$$

respectively. Both heat-flux and temperature excitations are considered and compared, to examine the possible differences in formulation on the obtained results. In practical experimental settings, these equivalent realizations of thermoacoustic perturbations are a consequence of the supplied electric power, which is not considered in the present gas-surface interaction analysis. The input signals are characterized by their common frequency ω^* and phase difference φ. To formulate a non-dimensional problem, the time-

scale $\omega^* - 1$ is used, together with the mean speed of sound c_0^* as the velocity scale. The characteristic length-scale is consequently c_0^* $/\omega^*$, of the order of the imposed acoustic wavelength. The density and temperature are non-dimensionalized by ρ_0^* and T_0^*, respectively, and the pressure by $\rho_0^* \mathscr{R}^* T_0^*$. In accordance with the Fourier law, the heat flux is normalized by $k_0^* T_0^* \omega^* / c_0^*$, where k_0^* is the gas co-efficient of heat conduction at equilibrium conditions.

Making use of the scaling introduced and linearizing about system equilibrium, the following $O(\varepsilon)$ unsteady one-dimensional balances of mass, momentum and energy are obtained:

$$\frac{\partial \rho}{\partial t} + \frac{\partial u}{\partial x} = 0, \tag{3}$$

$$\frac{\partial u}{\partial t} = -\frac{1}{\gamma}\left(\frac{\partial \rho}{\partial x} + \frac{\partial T}{\partial x}\right) + \frac{4}{3Re}\frac{\partial^2 u}{\partial x^2} \tag{4}$$

and

$$\frac{\partial T}{\partial t} = \frac{\gamma}{RePr}\frac{\partial^2 T}{\partial x^2} - (\gamma - 1)\frac{\partial u}{\partial x}, \tag{5}$$

respectively, for the density ρ, normal velocity u and temperature T perturbations. The acoustic pressure is given by the linearized form of the equation of state, $p = \rho + T$. In Eqs. (4) and (5),

$$Re = \frac{\rho_0^* c_0^{*2}}{\omega^* \mu_0^*}, \quad Pr = \frac{\mu_0^* c_p^*}{k_0^*} \text{ and } \gamma = \frac{c_p^*}{c_v^*}, \tag{6}$$

where Re and Pr mark the system effective Reynolds and Prandtl numbers, respectively. Here, μ_0^* denotes the gas mean dynamic viscosity, and c_p^* and c_v^* are the gas specific heat capacities at constant pressure and volume, respectively. The system of Eqs. (3)–(5) is supplemented by the wall impermeability condition,

$$u(x = 0) = \cos(t), \tag{7}$$

together with the normal heat-flux or temperature boundary conditions,

$$\frac{\partial T}{\partial x}\Big|_{x=0} = Q_\varepsilon \cos(t + \varphi) \text{ or } T(x = 0) = T_\varepsilon \cos(t + \varphi), \tag{8}$$

respectively. By applying the above, the boundary is assumed to be "ideal", in the sense that its mechanical and thermal properties are not coupled to the gas layer dynamics. Such effects may be taken into account in a more detailed modeling of the solid-gas interaction, yet are not in the scope of the present model. Problem formulation is completed by imposing far-field ($x \to \infty$) attenuation conditions for all perturbations.

In view of problem linearity and the time-harmonic form of the actuation signal, sinusoidal time dependence of all hydrodynamic fields is assumed,

$$F(t, x) = \overline{F}(x)\exp(it), \tag{9}$$

with the imaginary part omitted in the physical solution, and substituted into Eqs. (3)–(5) and (7), (8). This yields a system of ordinary equations,

$$i\overline{\rho} + \overline{u}' = 0, \quad i\overline{u} = -\frac{1}{\gamma}(\overline{\rho}' + \overline{T}') + \frac{4}{3Re}\overline{u}'',$$

$$i\overline{T} = \frac{\gamma}{RePr}\overline{T}'' - (\gamma - 1)\overline{u}', \tag{10}$$

where primes denote differentiations with respect to x, accompanied by wall-excitation boundary conditions,

$$\overline{u}(0) = 1 \text{ and } \overline{T}'(0) = Q_\varepsilon \exp(i\varphi) \equiv \widetilde{Q}_\varepsilon \text{ or } \overline{T}(0) = T_\varepsilon \exp(i\varphi) \equiv \widetilde{T}_\varepsilon, \tag{11}$$

and far-field attenuation conditions. The density and velocity perturbations may be eliminated using the mass and energy balances $\overline{\rho} = i\overline{u}'$ and

$$\overline{u} = -\frac{\gamma}{(\gamma - 1)RePr}\left(\frac{1}{\gamma} + \frac{4i}{3Re}\right)\overline{T}'' + \frac{1}{\gamma - 1}\left(i - \frac{4}{3Re}\right)\overline{T}', \tag{12}$$

to yield a single equation for the temperature,

$$a_2\overline{T}''' + a_1\overline{T}'' + a_0\overline{T} = 0, \tag{13}$$

where

$$a_2 = \frac{i\gamma}{RePr}\left(\frac{4}{3Re} - \frac{i}{\gamma}\right), \quad a_1 = -i\left(1 + \frac{4i}{3Re}\right) + \frac{\gamma}{RePr}, \quad a_0 = -i. \tag{14}$$

The biquadratic characteristic equation corresponding to Eq. (13) has four distinct roots, out of which only two have negative real parts that satisfy the far-field decay condition. Denoting

$$r_1 = \left[\frac{-a_1 - \sqrt{a_1^2 - 4a_2a_0}}{2a_2}\right]^{1/2} \quad \text{and} \quad r_2 = \left[\frac{-a_1 + \sqrt{a_1^2 - 4a_2a_0}}{2a_2}\right]^{1/2}, \tag{15}$$

the general attenuating solution for the transformed temperature perturbation is

$$\overline{T}(x) = D_1 \exp(r_1 x) + D_2 \exp(r_2 x). \tag{16}$$

The coefficients D_1 and D_2 are obtained by imposing the wall impermeability and heat-flux or temperature conditions (Eq. (11)). In the case of a heat-flux wall condition,

$$D_1^{(Q_\varepsilon)} = \frac{1 - \widetilde{Q}_\varepsilon(c_1 r_2^2 + c_2)}{c_1 r_1 (r_1^2 - r_2^2)} \quad \text{and} \quad D_2^{(Q_\varepsilon)} = \frac{\widetilde{Q}_\varepsilon - D_1^{(Q_\varepsilon)} r_1}{r_2}, \tag{17}$$

where

$$c_1 = -\frac{\gamma}{(\gamma - 1)RePr}\left(\frac{1}{\gamma} + \frac{4i}{3Re}\right) \quad \text{and} \quad c_2 = \frac{1}{\gamma - 1}\left(i - \frac{4}{3Re}\right). \tag{18}$$

In the case of a temperature boundary condition,

$$D_1^{(T_\varepsilon)} = \frac{(c_1 r_2^2 + c_2) r_2 \widetilde{T}_\varepsilon - 1}{(c_1 r_2^2 + c_2) r_2 - (c_1 r_1^2 + c_2) r_1} \quad \text{and} \quad D_2^{(T_\varepsilon)} = \widetilde{T}_\varepsilon - D_1^{(T_\varepsilon)}. \tag{19}$$

In following, the optimal conditions on the heat-flux or temperature perturbation parameters ($\widetilde{Q}_\varepsilon$ or $\widetilde{T}_\varepsilon$, respectively) to minimize the vibroacoustic pressure disturbance are sought by evaluating the large-Re approximation of the above expressions, and specifying a condition for the vanishing of the far acoustic field. The large-Re approximation is in line with the characteristically large Reynolds values (typically exceeding $Re \sim O(10^5)$), which are attained in experiments. Applying the $Re \gg 1$ limit to Eqs. (12)–(18) and taking $x \gg 1$, the temperature perturbation in Eq. (16) is found to be dominated by the r_1-exponential part, as

$$r_1 \approx -i\left(1 - \frac{i\gamma}{Re}\right) \quad \text{and} \quad r_2 \approx -\sqrt{iRePr}\left[1 - \frac{i}{Re}\left(\frac{1}{2}\left(-\frac{4}{3} - \frac{\gamma - 1}{Pr}\right) + \frac{2\gamma}{3}\right)\right].$$

Consequently, reverting to the time domain, the far-field approximation for the temperature perturbation is

$$T(x,t) \approx D_1 \exp\left[i(t - x) - \frac{\gamma x}{Re}\right]. \tag{20}$$

This describes a slowly decaying wave propagating away from the wall at the gas mean speed of sound and attenuating with an $O(Re^{-1})$ decay rate originating from viscous dissipation effects. Based on Eq. (12) and the linearized form of the equation of state, $p = \rho + T$, the far-field density, normal velocity and acoustic pressure are similarly proportional to D_1. To minimize the actuation-induced far-field signal, the vanishing of D_1 is therefore required, yielding the desired optimal values for the perturbation parameters $\widetilde{Q}_\varepsilon$ and $\widetilde{T}_\varepsilon$ to be calculated below.

Starting with Eq. (17) in the case of heat-flux thermal actuation, the optimal value for the heat-flux amplitude is found to be

$$\left|\widetilde{Q}_\varepsilon^{\text{opt}}(Re \gg 1)\right| = \left|(c_1 r_2^2 + c_2)^{-1}\right| \approx RePr. \tag{21}$$

A negative sign in the non-absolute-value form of $\widetilde{Q}_\varepsilon^{\text{opt}}$ should be added, indicating that heat needs to be inserted in an opposite phase to the vibroacoustic signal. Thus, heat should be removed when the boundary moves into the gas, and invested when the boundary is actuated outwards, specifying $\varphi^{\text{opt}} = \pi$. To formulate the above result in terms of the optimal ratio between thermal and kinetic energies supplied at the wall surface, dimensional expressions for the respective wall-inserted energies (per unit area) transferred to the gas during a time interval $t^* \in [0, t_f^*]$ are introduced. These are given by

$$E_k^* = \int_0^{t_f^*} p_0^* U_w^*(t^*) dt^* \quad \text{and} \quad E_q^{*(Q_\varepsilon)} = \int_0^{t_f^*} Q_w^*(t^*) dt^*, \tag{22}$$

respectively, where $p_0^* = \rho_0^* \mathscr{R}^* T_0^*$ marks the equilibrium gas pressure. Substituting Eqs. (1) and (2) into Eq. (22) and dividing, the required ratio is obtained as
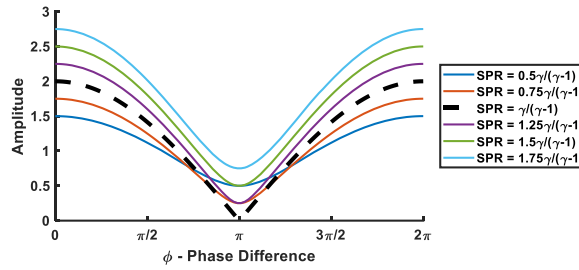
Fig. 1. Active noise cancellation performance of co-planar thermo- and vibro-acoustic emitters as a function of relative phase and different SPR.

$$\left.\left|\frac{E_q^{*(Q_\varepsilon)}}{E_k^*}\right|^{\mathrm{opt}}\right|_{Re\gg1} = \frac{\gamma}{(\gamma-1)RePr}\left|\widetilde{Q}_\varepsilon^{\mathrm{opt}}(Re\gg1)\right| = \frac{\gamma}{\gamma-1}. \tag{23}$$

Considering the wall temperature excitation case, $D_1^{(T_\varepsilon)}$ in Eq. (19) is set to zero, yielding

$$\left|\widetilde{T}_\varepsilon^{\mathrm{opt}}(Re\gg1)\right| = \left|\left[r_2\left(c_1 r_2^2 + c_2\right)\right]^{-1}\right| \approx \sqrt{RePr}. \tag{24}$$

To compare the result in Eq. (24) with the optimal ratio required between wall-inserted thermal and kinetic energies found in Eq. (23), it is convenient to consider the system from a thermodynamic point of view. To this end, a "virtual" adiabatic piston is placed in the far-field, and the first law of thermodynamics is applied. Assuming quasistatic conditions (prevailing at $Re \to \infty$), the dimensional energy balance reads

$$c_p^* dT^* = p_0^* dv^* + c_v^* dT^*, \tag{25}$$

equating the amount of heat invested in the system with the sum of work done by the moving surfaces and the total change in system internal energy. Here, dT^* directly measures the temperature variation applied at the wall. In the case of an oscillating adiabatic surface, the balance (25) becomes trivial, as no heat enters the system, and the net amount of work done by the gas is zero, with both animated and "virtual" boundaries moving in parallel motion. However, the balance changes when considering the thermoacoustic problem of a heated stationary surface. Here, using Eq. (25) and the relation $\mathscr{R}^* = c_p^* - c_v^*$ for an ideal gas, the ratio between the amount of heat transferred at the thermally-excited wall and the work done by the moving far-field piston yields the required optimal ratio in the quasistatic limit,

$$\left.\left|\frac{E_q^{*(T_\varepsilon)}}{E_k^*}\right|^{\mathrm{opt}}\right|_{Re\gg1} = \frac{c_p^* dT^*}{\mathscr{R}^* dT^*} = \frac{\gamma}{\gamma-1}. \tag{26}$$

This can be referred to as the relative part of inserted thermal energy transmitted into sound in the far field, which is expectedly equal to the value in the heat-flux-excitation problem calculated in Eq. (23).

Beyond predicting the optimal ratio of energies between the two sources, the above framework enables to easily study the coupled performance of the vibro-acoustic and thermo-acoustic emitters in various conditions. Fig. 1 depicts this performance in terms of aggregate normalized acoustic signal amplitude as a function of relative phase between the sources and different sources' powers ratio (SPR). It can be observed that only at SPR of $\gamma/(\gamma-1)$, full cancellation is indeed possible when the phases of the two sources are reversed (black dashed line in Fig. 1).

3. Experimental system and procedure

3.1. Acoustic system

The analytical predictions are validated experimentally using a specially designed acoustic system, which includes two separate acoustic emitters and is instrumented for required measurements. The first source of the system is a vibro-acoustic transducer, built using MSE Audio SolidDrive SD1 actuator that is attached to a thin metallic plate. The second source is a thermo-acoustic device built from a $100 \times 100 \times 2\cdot10^{-4}$ mm golden thermophone layer and 1 mm-thick aluminum nitride (AlN) substrate. The two devices are sandwiched in a single structure with a layer of gypsum plaster insulation between them. In addition, the acoustic system is instrumented with a K-type thermocouple, which is also embedded in the assembly to measure the substrate backing temperature, and with a Wilcoxon 736 high sensitivity accelerometer, which measures the vibrations of the metallic plate. The setup is described schematically in Fig. 2 (left). A photo of exposed experimental acoustic system surrounded by a layer of acoustic insulation appears in Fig. 2 (right).

The structure is placed in a sealed anechoic chamber that includes additional sensors and enables to measure acoustic cancellation properties in different gases. The installed measurement devices include two pre-amplified GRAS 40BE condenser microphones, K-type thermocouple for measurement of gas temperature close to thermophone surface and Huba Control 528 chamber pressure gauge. One of the microphones is mounted at a constant distance of 440 mm from the thermophone transducer surface, whereas the other one is
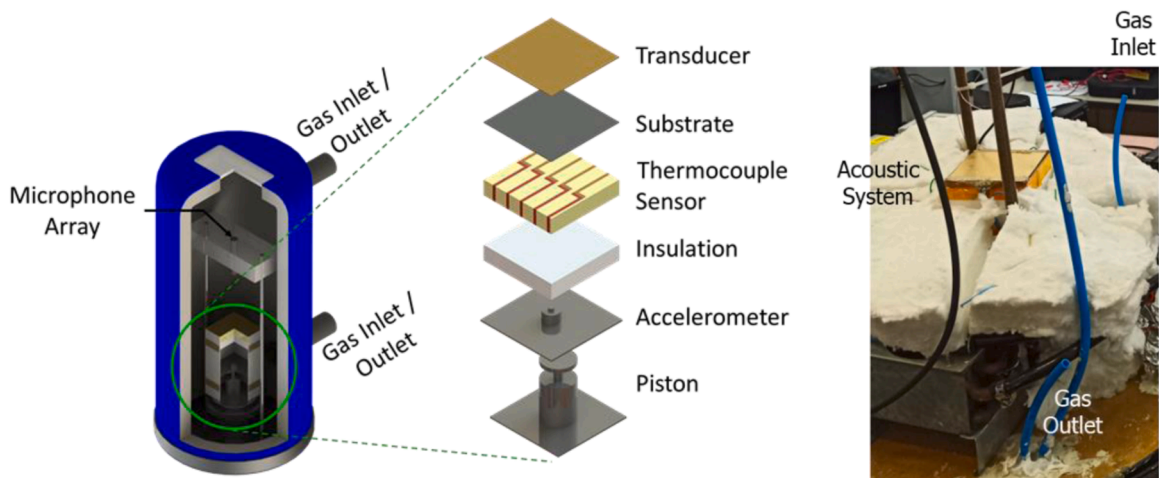
Fig. 2. Structure of the thermo-vibro-acoustic experimental setup (left) and photo of experimental system with acoustic insulation around it (right).
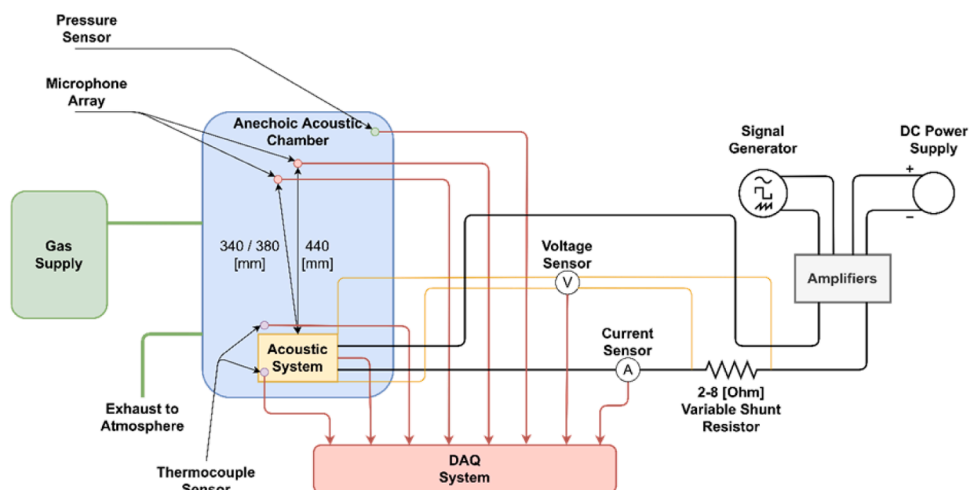

Fig. 3. Schematic of the active noise cancellation demonstrator facility.

traversable within distance range of $[340, 380]$ mm. The locations of the microphones are selected to ensure that all measurements are conducted in far-field conditions for the implemented excitation frequency [23,24].

3.2. Test facility

The overall structure of the active noise cancellation demonstrator facility is summarized schematically in Fig. 3. The vibro- and thermo-acoustic sources are powered by synchronized sine signals with controllable relative phase, produced by Tektronix AFG3102 function generator. In the case of the vibro-acoustic loudspeaker, the signal is boosted via MSE Audio SolidDrive SD-250 amplifier, whereas the thermo-acoustic transducer is connected to a Lanzar Vector VCT-2610 6 kW amplifier via $2 - 8$ Ω, 1 kW protective variable shunt resistor.

In addition to sensors placed within the anechoic chamber, the setup is also instrumented with voltage and current meters that measure the power delivered into the acoustic sources. All relevant signals are sampled using NI cDAQ-9189 chassis and a set of data acquisition modules. The microphones and the accelerometer are connected via Endevco 133 signal conditioner to a high-speed NI-9223 analog acquisition module, with sampling frequency of up to 1 MS/s/ch. The voltage readings and the current sensors (Riedon SSA-100) are connected to the same card. The thermocouples are recorded via NI-9211 card and the pressure sensor is read through NI-9209 module. The system and data acquisition are controlled via an in-house developed LabVIEW code and the data is subsequently post-processed in MATLAB. The accuracies and specifications of all sensors are summarized in Table 1.

Table 1

Specifications of measurement equipment - active noise cancellation facility.

Type	Device	Range	Accuracy
Data Acquisition	NI-9209	± 10 V	Reading - 0.06% Full Scale - 0.003%
	NI-9223	± 10 V	Reading - 0.02% Full Scale - 0.01%
	NI-9211	± 80 mV	K-type - $\sim 1.2°$C
Sensor	Riedon SSA-100	± 100 A	Reading - 0.1%
	GRAS 40BE and GRAS 26CB-HT	Up to 40 kHz $[35, 160]$ dB	Reading - 0.5% (Endevco 133)
	Wilcoxon 736	50 g	Reading - 5% Full scale - 150 μg
	Huba Control 528	$[0, 1.6]$ barg	Full scale - 0.5%
	K-type Thermocouple	$[-270, 1260]°$C	Greater among 2.2°C or 0.75%

Table 2

Data acquisition parameters for the noise cancellation demonstrator facility.

Parameter	Checked Range	Step	Selected Value
Sine Wave Frequency	$[4, 15]$ kHz	10 Hz	11850 Hz
Sampling Rate	$[100, 1000]$ kS/s	–	500 kS/s
Sample Duration	$[0.1, 1]$ s	0.1 s	0.2 s
Phase Switching Time	$[0.1, 1]$ s	0.1 s	0.5 s

3.3. Experimental procedure

In all conducted experiments, the thermo-acoustic source is supplied with a constant average power input of 50 W and its acoustic output is measured to provide reference SPL value. Then, the thermophone is turned off and the SolidDrive actuator is activated and tuned to generate same SPL. The gain of the SolidDrive amplifier is kept constant and the control over its output is achieved via variation of input voltage. In the scope of the available acoustic setup, global sound cancellation is not feasible in any given frequency due to several reasons. First, the two acoustic emitters are not infinite and are not fully co-planar. Instead, there are several layers of insulation and measurement components sandwiched between the two sources. Therefore, the system also has some damping associated with its complex structure. Overall, global cancellation only becomes feasible if done at the frequency of the rigid body motion, when the entire assembly can move as a single solid mass.

The rigid body motion frequency is determined by conducting preliminary measurements in the air, where the signals generated by the SolidDrive and thermophone transducers are swept within the range of $[4, 15]$ kHz (the frequency of the thermophone input signal is half of the generated sound's). At each frequency, the relative phase of the two sources is varied. The phase-frequency sweeps are initially done with steps of 1 kHz, with gradual increase of resolution up to 10 Hz in the potentially favorable regions. The existence of global cancellation is confirmed by comparing the measurements of the static and the traversed microphones, where the phases of destructive interference (maximal reduction of the sensed acoustic level) match for both microphones irrespective of their relative location above the sound-generating surface. Through this methodology, the optimal frequency is determined to be 11850 Hz. In following, the traversing microphone is then fixed at its highest position for all subsequent measurements.

Beyond identification of global acoustic cancellation frequency, the relevant acquisition parameters that are determined prior to experimental campaign include data acquisition rate, duration of each acquired sample, and rest time before acquisition after each switch of phases. Optimal sample duration and phase switching time that result in highest quality of data are checked at the global cancellation frequency within the range of $[0.1, 1]$ s with steps of 0.1 s. Their optima are found to be 0.2 s and 0.5 s, respectively. The acquisition rate is set to 500 kS/s for all relevant channels (microphones, accelerometer, voltages and currents) to obtain high-fidelity data while keeping the size of the saved data files within manageable bounds. The selected data acquisition parameters are summarized in Table 2.

During the experimental campaign, the outputs of the two acoustic sources are synchronized and triggered simultaneously, while the relative phase between their input signals is variated within the range of $[-2\pi, 2\pi]$ with steps of $\pi/18$. In practical terms, this is represented by keeping the input phase of the thermophone channel constant, while altering the phase of the SolidDrive input channel. After acquiring the data, it undergoes Fast Fourier Transform (FFT) to recover amplitude content at the excitation frequency. Towards validating signal periodicity during each measurement, the negative phase values are modulated to span $[0, 2\pi]$.

Since the thermo- and vibro-acoustic sources are powered by separate electronic circuits, their relative phase delay can differ during the separate amplification processes. Hence, the relative phase of the signal outputs may not necessarily correlate to the to the relative phase of the signal input, prescribed by the function generator. Therefore, the actual phase difference is decoupled by conversion of the temporal current signals measured at the inputs of the two emitters to frequency domain via FFT and calculation of their relative phase angle. The difference between the two approaches is charted in Fig. 4 for a representative measurement, where the left dataset corresponds to measured SPL as a function of input phase prescribed by function generator, whereas the right chart correlates the measured aggregate acoustic signal to the output phase decoupled from current sensor measurements. Slight, but distinguishable differences, are apparent in the two depictions. The data in the chart describes the acoustic signal recorded from the two microphones as a response to an aggregate excitation from both thermo-acoustic and vibro-acoustic emitters as a function of the relative phase between the sources. At the point of optimal cancelation (reversed phase between the two sources), the recorded SPL exhibits
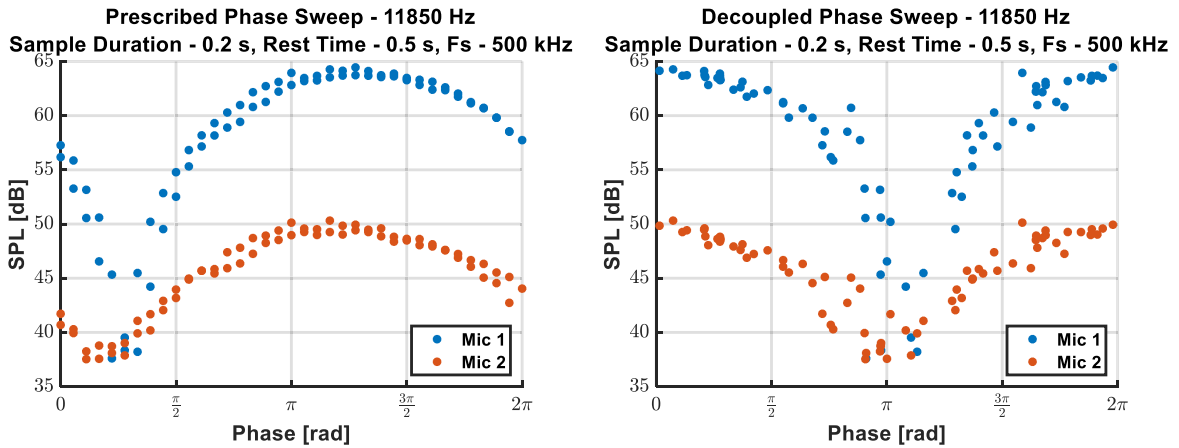
Fig. 4. Measured SPL as a function of prescribed (left) and extracted (right) relative phase between the two acoustic sources for representative measurement, where global cancellation is observed when the relative phase of the two sources is reversed.
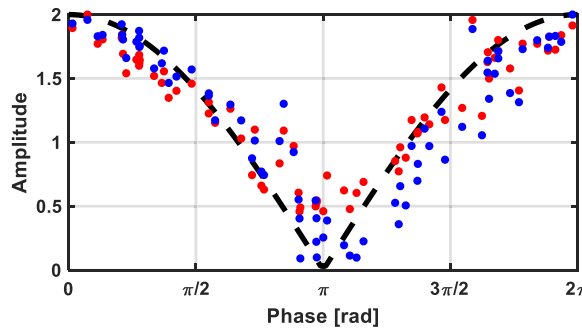

Fig. 5. Comparison between analytic model and representative measurements in Fig. 4 in terms of normalized amplitude as a function of phase difference.

significant drop to below 40 dB, indicating that one source has successfully cancelled the other. Since both microphones show this behavior at the same relative phase, regardless of their distance from the source, the conclusion is that the cancellation indeed happens in a global sense rather than locally.

Moreover, this representative data can also be used to directly corroborate the developed analytic model. This comparison is charted in Fig. 5, where the data sampled from both microphones is converted from dB to linear axis and is normalized to account for the difference in their distance from the source. The measurements from both microphones (blue and red points in Fig. 5) collapse to same line, which corresponds to SPR of $\gamma/(\gamma-1)$ (black dashed line in Fig. 1).

Due to limitations of experimental setup (damping, noncoplanar and finite sources), true rigid body motion of the acoustic system is not always attainable. Therefore, some of the taken measurements would not attain global cancellation and would only allow to observe local destructive interference, where the amplitudes measured by the two microphones would drop at different phases. Since the present work only deals with global noise cancellation and formulates prediction of sources' power ratio in this condition as a function of the surrounding media, points of local cancellation are irrelevant and have no further value for subsequent data post-processing. Hence, the quality of all sampled data is evaluated through proximity of decoupled minimal and maximal phases in the measurements obtained from the two microphones. This step includes normalization of the measured data into $[0, 1]$ range and application of cross-correlation ("⋆" operator), without temporal displacement, to obtain quantitative index for the closeness of signals in each set of measurements. The data is sampled in four different gases, selected due to the differences in their respective specific heat ratios: Argon (Ar) - $\gamma = 1.66$, Nitrogen (N$_2$) - $\gamma = 1.4$, Carbon Dioxide (CO$_2$) - $\gamma = 1.28$, and Norflurane (R134a) - $\gamma = 1.2$. 40 phase sweeps are performed in each gas at constant thermophone power input. To ensure repeatability of results, the data is measured in 2 separate batches of 20 samples. Finally, 20% of all measurements (8 samples for each gas) with highest closeness index (best-pronounced global cancellation features) are retained for further data reduction and analysis. The data selection process is described graphically in Fig. 6, where the red and blue lines schematically represent SPL vs. decoupled phases of the two microphones. After scaling, the top synthetic dataset does not indicate global cancellation and is therefore unused in future analysis, whereas the bottom exemplary data is kept.
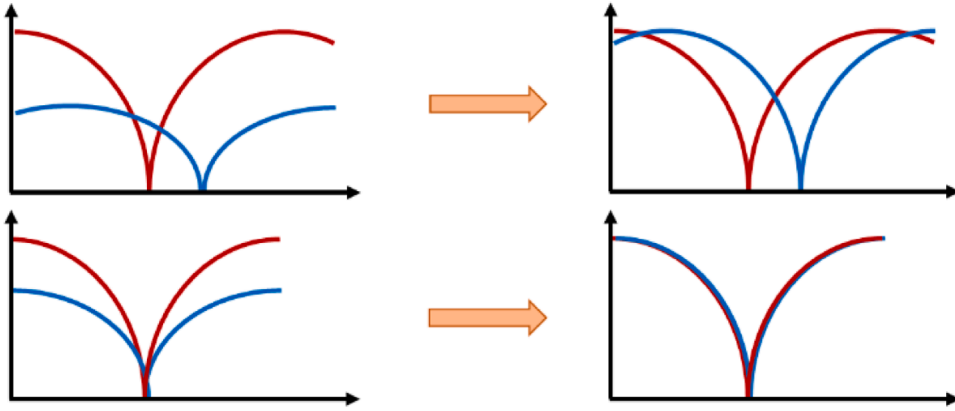
Fig. 6. Graphic representation of global cancellation wellness estimation, where the measurements in the top synthetic dataset are not close and are therefore rejected, while the bottom exemplary measurements are retained.

Table 3
Shomate equation coefficients for different gases.

Fluid	a_0	a_1	a_2	a_3	a_4
Ar	0.786	$< 10^{-10}$	$< 10^{-10}$	$< 10^{-10}$	-0.037
N_2	28.986	0.002	$-9.647 \cdot 10^{-6}$	$1.664 \cdot 10^{-8}$	117
CO_2	24.997	0.055	$-3.369 \cdot 10^{-5}$	$7.948 \cdot 10^{-9}$	$1.366 \cdot 10^5$
R134a	19.4	0.259	$-1.297 \cdot 10^{-4}$	0	0

3.4. Data reduction

After sifting the measurements for highest-quality data, the remaining data sets are post-processed to evaluate their dependency on the specific heat ratio of the different gases. However, although the analytical findings indicate that the ratio of thermal and kinetic energies, and therefore also ratio of powers (PW_q/PW_k) delivered by the thermo-acoustic and vibro-acoustic sources during mutual cancellation, respectively, is correlated to $\gamma/(\gamma - 1)$, it is impossible to obtain PW_q directly in the experiment and the electric power delivered into the thermophone (PW_e) is measured instead. It is therefore hypothesized that the two values are related via

$$PW_q = PW_e \cdot f_1(\eta) \cdot f_2(e), \tag{27}$$

where $f_1(\eta)$ is a function of efficiency that accounts for the conversion of electrical energy into heat flux and $f_2(e)$ is the thermal power split that describes that amount of thermal power that leaves the thermophone into the surrounding fluid with respect to the overall generated heat.

Although the efficiency η typically depends on frequency, geometry, thermo-acoustic transducer structure and supplied power, in the scope of the present research it and its function are assumed to be constant since all experiments are done at same excitation frequency with constant input power and using the same acoustic system. Assuming that there is no heat remaining trapped in the thermophone layer, the thermal power split is described by [17]

$$f_2(e) = \frac{e_f}{e_f + e_{\text{sub}}}, \tag{28}$$

where e is the thermal effusivity ($e = \sqrt{\rho C_P \kappa}$) and the subscripts f and sub relate the fluid and substrate layers, respectively. The density, specific heat capacity and thermal conductivity (and, therefore, effusivity) of the substrate are considered to be constant (the values for AlN are taken from [25]). The gas density is evaluated from gas pressure and temperature measurements via ideal gas law ($\rho = p/\mathscr{R}T$), whereas the specific heat capacity of the gas is calculated as a function of temperature using Shomate equation [26]:

$$C_P^0 = a_0 + a_1 T + a_2 T^2 + a_3 T^3 + a_4 T^{-2}. \tag{29}$$

In this equation, a_i are gas-dependent coefficients and C_P^0 is the molar specific heat capacity ($C_P = C_P^0/MW$, where MW is the molar mass of the gas). In the case of argon, nitrogen and carbon dioxide, the coefficients are available from data published by NIST [26], whereas the coefficients for norflurane are published by DuPont [27]. The coefficient values used in the scope of the present effort are summarized in Table 3. Although thermal conductivities of different gases also have temperature dependency, it is negligible in the temperatures observed in the scope of experiments ($T_{gas} < 350$ K) and the thermal conductivity values are assumed to be constant ($\kappa_{Ar} = 0.016$ W/mK, $\kappa_{N_2} = 0.024$ W/mK, $\kappa_{CO_2} = 0.015$ W/mK, and $\kappa_{R134a} = 0.019$ W/mK).
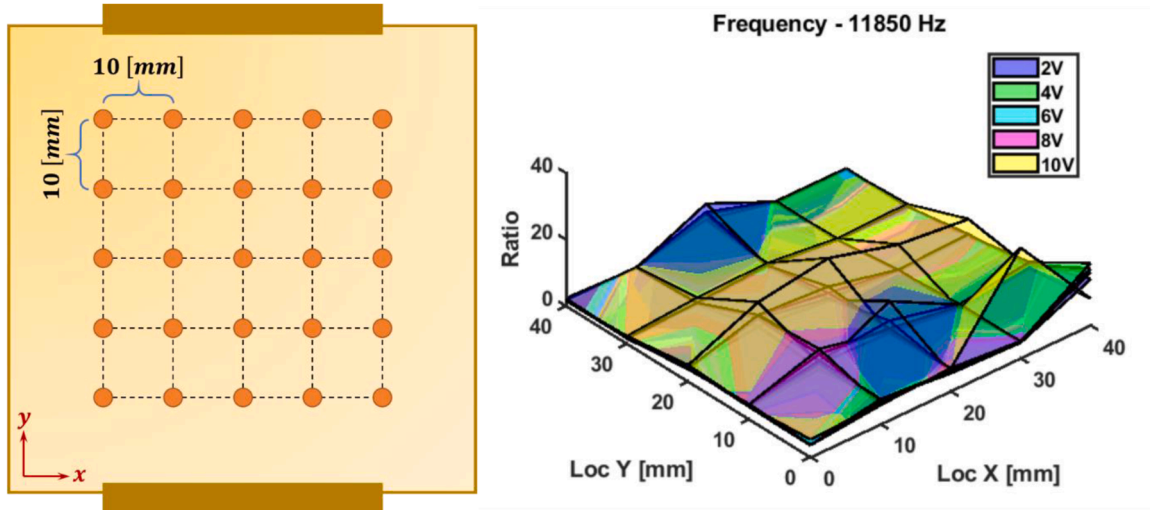
Fig. 7. (Left) Accelerometer calibration grid, where orange dots indicate the different vibrometer measurement locations, and (right) Ratio of accelerometer and vibrometer readings across the sound-generating surface at frequency of 11850 [Hz] and SolidDrive input voltage in the range of $[2, 10]$ $[V]$.

To complete the calculation, the average power input of the thermophone transducer is divided by the kinetic power produced by the vibration of the sound-generating surface:

$$\text{PW}_k = p \cdot v \cdot A, \tag{30}$$

where v is the RMS value of the surface velocity obtained from integration of accelerometer reading and A is the surface area. The power ratio can now be rewritten as

$$\frac{\text{PW}_q^{\text{opt}}}{\text{PW}_k} \approx \frac{\text{PW}_e^{\text{opt}}}{\text{PW}_k} \cdot f_1(\eta) \cdot \frac{e_f}{e_f + e_{\text{sub}}}. \tag{31}$$

Using this formulation, the data from experimental campaign can be analyzed to confirm whether the power ratio is indeed correlated to the value of γ as suggested in Eqs. (23) and (26), namely

$$\frac{\text{PW}_q^{\text{opt}}}{\text{PW}_k} = \frac{\gamma}{\gamma - 1}. \tag{32}$$

3.5. Sensor calibration and uncertainty estimation

Before starting the experimental campaign, several of the sensors undergo calibration process. First, the response linearity of the pressure sensor (Huba Control 528) is validated using Additel 912A low pressure test pump with adjustment resolution of up to 0.1 Pa and high-accuracy Additel 681 gauge with range of up to 3.5 bar and full-scale accuracy of 0.02%. Then, the two microphones are calibrated in all experimental gases using GRAS 42AB calibrator. For consistency, the acoustic chamber of the calibration unit is first fully vented in each gas, and only then the microphones are placed into it. During calibration, the microphones sensitivities are recorded to be constant, regardless of the gaseous media - this observation is consistent with the operating principle of a condenser microphone, which changes its capacitance in response to externally applied pressure. Therefore, if the microphone venting port is located in same environment, the produced signal is not affected by the media, but rather by the present acoustic pressure.

The last step in the sensors' calibration procedure is associated with the accelerometer. As the accelerometer is placed deep inside the compound acoustic system, it is only capable of providing acceleration readings from its immediate location on the metallic plate. However, to evaluate the ratio between the thermal power supplied into the thermophone and the vibrations induced by the conventional loudspeaker, actual front surface movements must be determined. Therefore, prior to the main experimental measurements, a vibrometer is used to record the surface motion in an open setup excited at a relevant frequency with a range of SolidDrive input voltages. The accelerometer readings are also recorded and as the closed test system does not allow for optical measurements, the ratio of the two readings serves as accelerometer calibration during the experiments.

The used laser vibrometer system includes a Polytec VibroFlex VFX-F-110 front-end and a VibroFlex Xtra VFX-I-120 sensor head, equipped with a VFX-O-100 Mini Fiber optic system. In this configuration, the vibrometer is able to decode acceleration in the ranges of $[10, 10^8]$ m/s with a frequency of up to 3 MHz. During calibration, the vibrometer sensor is placed 300 mm above the planar acoustic source on a linear traverse stage. The system is then used to measure the planar surface movement as a response to excitation by SolidDrive transducer at the selected frequency (11850 Hz) with SolidDrive input voltage in the range of $[2, 10]$ V with 2 V steps.
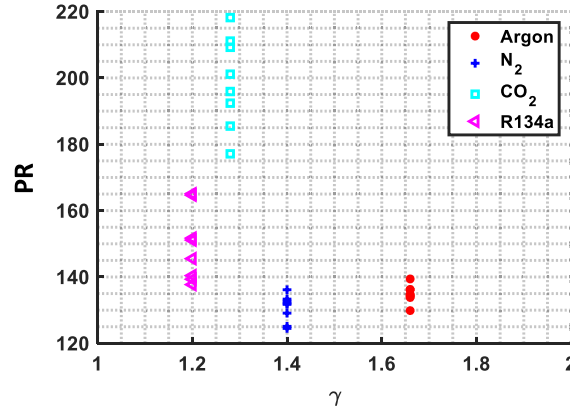
Fig. 8. Experimentally obtained ratio of powers as a function of heat capacity ratio, where the gases are denoted by different markings.

The surface is sampled in a 40 × 40 mm grid with a step of 10 mm (total of 25 sample points for each voltage-frequency pair), Fig. 7 (left). At each point, the vibrometer and the accelerometer signals are sampled and stored for 6 s with a sampling frequency of 1 MS /s. The data is then converted to frequency domain using FFT algorithm to obtain vibration amplitude readings and their ratio at the relevant frequency.

Charting the measured acceleration ratios for the different SolidDrive voltage inputs in three-dimensional space, Fig. 7 (right), it can be observed that beyond several irregularities introduced at 2 or 10 V input (blue and yellow surfaces, respectively), the surface response is relatively flat and uniform in the input range of [4, 8] V. This is corroborated by the close average acceleration ratio at different voltages ($RA_{avg@4V} = 5.1$, $RA_{avg@6V} = 5.05$ and $RA_{avg@8V} = 4.97$) and further supports the observation that selected excitation frequency correlates with solid body motion. Therefore, by limiting the input voltage that is applied to SolidDrive transducer during the experiment to the range of [4, 8] V, it is possible to use a single average value that represents the gain of the accelerometer with respect to the actual movement of the sound-producing surface - $RA_{avg@11850Hz} = 5.042$. This value is then used to estimate the surface velocity (v in Eq. (30)) from the measured vibrations of the metallic plate via

$$v = \int \frac{a}{RA_{avg}} dt, \tag{33}$$

where a is the measured acceleration.

The uncertainties of the reported findings are evaluated according to a standard methodology suggested by National Institute of Standards and Technology [28]. The purpose of this technique is to calculate how the uncertainty in each of the directly measured variables $x_1, x_2, ..., x_n$ propagates into the value of the calculated quantity $y = f(x_1, x_2, ..., x_n)$. Then, the uncertainty of the calculated quantity (U_y) can be determined as a function of the measured variables' uncertainties ($U_{x,i}$) via:

$$U_y = \sqrt{\sum_{i=1}^{n} \left(\frac{\partial y}{\partial x_i}\right)^2 . U_{x,i}^2}. \tag{34}$$

According to this approach, the accuracy of the experimentally measured kinetic, electric and thermal powers are all estimated to be below ±0.2%. The accuracy of the reported kinetic power includes contributions associated with accelerometer and pressure measurements, whereas the electric power accuracy relates to sources of error associated with voltage and current measurements. Finally, the systematic error on the reported thermal power is also affected by the accuracy of the thermocouple readings. Beyond these values, the uncertainties of the power ratio calculations seem to be dominated by the precision error (exhibiting a minor spread), resulting from the difficulty in sustaining "steady-state conditions" for the acquisition time interval. In particular, transient heating of the substrate and the surrounding gas has a direct influence on the performance of the thermophone.

4. Results

The power ratios measured in the scope of the experimental campaign are charted in Fig. 8 as a function of the specific heat capacity ratio (γ). Henceforth, the different gases used in the experiments are denoted by different marker colors (Ar - red circles, N_2 - blue crosses, CO_2 - turquoise squares, and R134a - purple triangles). The data can be compared using coefficient of variance (CV - the ratio of the standard deviation to the mean), where in this case, direct comparison of measured power ratios (electric-to-kinetic) yields a relatively large spread (CV ≈ 19%).

In following, the γ-function $g(\gamma) = (\gamma - 1)/\gamma$ is factored in to estimate its effect on the spread of data and evaluate whether the ratio of electric and kinetic powers behaves in a similar manner to the ratio of thermal and kinetic powers:
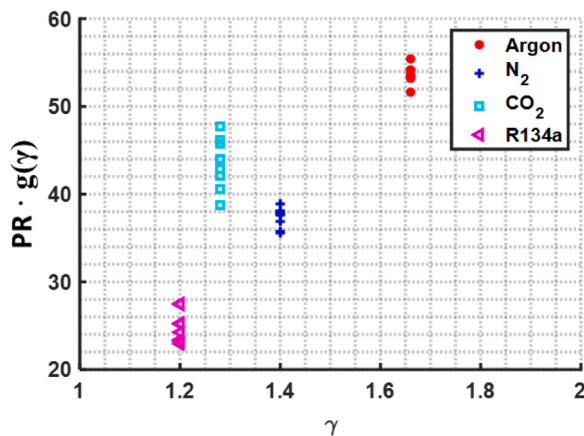
Fig. 9. Ratio of powers multiplied by γ-function with respect to heat capacity ratio.
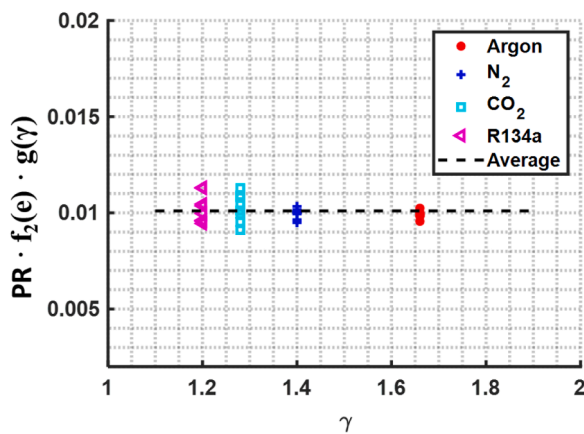
Fig. 10. Factoring of thermal power split results in collapse to a constant value, regardless of the gas.
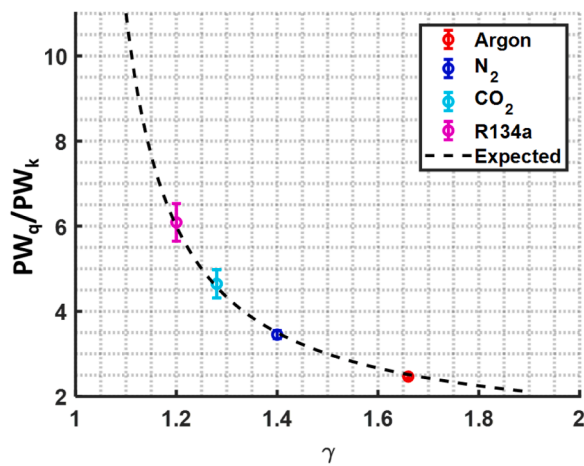
Fig. 11. Experimentally measured (markers) and theoretically predicted (dashed line) thermal and kinetic power ratio as a function of heat capacity ratio.

$$\frac{PW_e^{\text{opt}}}{PW_k} = \frac{\gamma}{\gamma - 1} \quad \rightarrow \quad \frac{PW_e^{\text{opt}}}{PW_k} \cdot \frac{\gamma - 1}{\gamma} = \text{const.} \tag{35}$$

This analysis is summarized in Fig. 9, where the data is observed to have an even larger spread and CV $\approx$ 27%. Finally, when the thermal power split calculated based on the measured gas temperature,

$$f_2\left(e, T_{\text{gas}}\right) = \frac{e_f\left(T_{\text{gas}}\right)}{e_f\left(T_{\text{gas}}\right) + e_{\text{sub}}}, \tag{36}$$

is also considered, the experimental data collapses to a single constant value (CV $= 5.4\%$), regardless of the media used in experiments, dashed line in Fig. 10. Substituting this value into the calculation to account for the electro-thermal conversion process efficiency and other experimental constants, the final comparison of the measured and theoretically predicted values is then made in Fig. 11, where the data obtained from experiments is denoted by colored markers and the theoretical curve is depicted by the dashed line. The bounds of experimental datapoints represent the spread of values observed during the individual experiments (drift of steady state conditions) in each gas and the prior analytical findings are seen to be fully supported by the experimental data obtained in the scope of measurements.

If divided by the pressure generated from a vibro-acoustic source, the results of other studies that established various acoustic pressure formulations for the thermophone emitter output [5,16–18] infer that the ratio of the sources' powers should correspond to $c_v/\mathscr{R} = 1/(\gamma - 1)$ in the case of co-planar acoustic cancellation. Clearly, this approach would not collapse the experimental data to a single value as depicted in Fig. 10, considering that a factor of γ exists between these prior findings and the presently portrayed relation of $c_p/\mathscr{R} = \gamma/(\gamma - 1)$, demonstrated both theoretically and experimentally.

5. Summary and conclusions

The present research effort analyzes the feasibility of thermo-acoustic emitters to serve as boundary sources for global noise cancellation. Moreover, the characteristics of this active cancellation approach are studied as a function of the surrounding gaseous media.

First, an acoustic system is built from co-planar thermo- and vibro-acoustic sources and is placed in an instrumented sealed chamber. Then, after calibration of relevant sensors, global active noise cancellation is observed via measurements of two microphones in several gases with large variation of specific heat capacity ratios (argon, nitrogen, carbon dioxide and norflurane). Finally, the sampled data is post-processed and compared with the analytical model predictions.

The analysis of data indicates that the ratio of thermal-to-kinetic powers corresponds to the theoretically derived value of $\gamma/(\gamma - 1)$, after considering the thermal power split between the gas and the substrate. Moreover, the ensuing collapse of the sampled data from different gases to a singular value corroborates the validity of the initial constant efficiency assumption for the electro-thermal conversion process. In particular, within the field of active sound cancellation, the present experimental validation proves feasibility of global - rather than local - noise reduction, which is significantly less practical with conventional vibro-acoustic devices.

CRediT authorship contribution statement

Boris Leizeronok: Methodology, Software, Validation, Investigation, Writing – original draft, Writing – review & editing, Visualization. **Alex Kleiman:** Software, Investigation, Writing – original draft. **Shimon Julius:** Methodology, Validation. **Avshalom Manela:** Conceptualization, Formal analysis. **Beni Cukurel:** Conceptualization, Validation, Resources, Writing – original draft, Writing – review & editing, Supervision, Project administration, Funding acquisition.

Declaration of Competing Interest

The authors declare no conflict of interest.

Data availability

Data will be made available on request.

Acknowledgements

References

[1] F. Braun, Notiz über Thermophonie (Note about thermophony, Ann. Phys. 301 (6) (1898) 358–360, https://doi.org/10.1002/ANDP.18983010609.
[2] P. De Lange, On thermophones, Proc. R. Soc. Lond. Ser. A 91 (628) (1915), https://doi.org/10.1098/rspa.1915.0015. *Contain. Pap. a Math. Phys. Character.*
[3] H. Hu, Y. Wang, Z. Wang, Wideband flat frequency response of thermo-acoustic emission, J. Phys. D Appl. Phys. 45 (34) (2012), 345401, https://doi.org/10.1088/0022-3727/45/34/345401.

[4] H.D. Arnold, I.B. Crandall, The thermophone as a precision source of sound, Phys. Rev. 10 (1) (1917) 22–38.
[5] L. Xiao, et al., Flexible, stretchable, transparent carbon nanotube thin film loudspeakers, Nano Lett. 8 (12) (2008) 4539–4545, https://doi.org/10.1021/NL802750Z.
[6] H. Shinoda, T. Nakajima, K. Ueno, N. Koshida, Thermally induced ultrasonic emission from porous silicon, Nature 400 (6747) (1999) 853–855, https://doi.org/10.1038/23664.
[7] R.R. Boullosa, A.O. Santillan, Ultrasound radiation from simple thermoacoustic transducers, Acta Acust. United Acust. 90 (2) (2004) 277–284.
[8] T.M. Bouman, A.R. Barnard, M. Asgarisabet, Experimental quantification of the true efficiency of carbon nanotube thin-film thermophones, J. Acoust. Soc. Am. 139 (3) (2016) 1353, https://doi.org/10.1121/1.4944688.
[9] A.E. Aliev, Y.N. Gartstein, R.H. Baughman, Increasing the efficiency of thermoacoustic carbon nanotube sound projectors, Nanotechnology 24 (23) (May 2013), 235501, https://doi.org/10.1088/0957-4484/24/23/235501.
[10] A.R. Barnard, D.M. Jenkins, T.A. Brungart, T.M. McDevitt, B.L. Kline, Feasibility of a high-powered carbon nanotube thin-film loudspeaker, J. Acoust. Soc. Am. 134 (3) (2013) EL276, https://doi.org/10.1121/1.4817261.
[11] A.O. Niskanen, J. Hassel, M. Tikander, P. Maijala, L. Grönberg, P. Helistö, Suspended metal wire array as a thermoacoustic sound source, Appl. Phys. Lett. 95 (16) (2009), 163102, https://doi.org/10.1063/1.3249770.
[12] E.C. Wente, The thermophone, Phys. Rev. 19 (4) (1922) 333, https://doi.org/10.1103/PhysRev.19.333.
[13] A.E. Aliev, M.D. Lima, S. Fang, R.H. Baughman, Underwater sound generation using carbon nanotube projectors, Nano Lett. 10 (7) (2010) 2374–2380, https://doi.org/10.1021/NL100235N.
[14] L. Xiao, et al., High frequency response of carbon nanotube thin film speaker in gases, J. Appl. Phys. 110 (8) (2011), 084311, https://doi.org/10.1063/1.3651374.
[15] M. Daschewski, Thermophony in Real Gases: Theory and Applications, Universität Potsdam, 2016.
[16] M. Daschewski, R. Boehm, J. Prager, M. Kreutzbruck, A. Harrer, Physics of thermo-acoustic sound generation, J. Appl. Phys. 114 (11) (2013), 114903, https://doi.org/10.1063/1.4821121.
[17] H. Hu, T. Zhu, J. Xu, Model for thermoacoustic emission from solids, Appl. Phys. Lett. 96 (21) (2010), 214101, https://doi.org/10.1063/1.3435429.
[18] S.S. Asadzadeh, A. Moosavi, C. Huynh, O. Saleki, Thermo acoustic study of carbon nanotubes in near and far field: theory, simulation, and experiment, J. Appl. Phys. 117 (9) (2015), 095101, https://doi.org/10.1063/1.4914049.
[19] C.H. Hansen, Understanding Active Noise Cancellation, 1st ed., CRC Press, 2001.
[20] A. Manela, L. Pogorelyuk, Cloaking via heating: Approach to acoustic cloaking of an actuated boundary in a rarefied gas, Phys. Fluids 26 (6) (2014), 062003, https://doi.org/10.1063/1.4884369.
[21] A. Manela, L. Pogorelyuk, Active noise control of a vibrating surface: Continuum and non-continuum investigations on vibroacoustic sound reduction by a secondary heat-flux source, J. Sound Vib. 358 (2015) 20–34, https://doi.org/10.1016/J.JSV.2015.08.016.
[22] S. Julius, R. Gold, A. Kleiman, B. Leizeronok, B. Cukurel, Modeling and experimental demonstration of heat flux driven noise cancellation on source boundary, J. Sound Vib. 434 (2018) 442–455, https://doi.org/10.1016/J.JSV.2018.02.007.
[23] D.A. Bies, Uses of anechoic and reverberant rooms, Noise Control Eng. J. 7 (1976) 154–163.
[24] S. MacDonald, Sound Fields: Free versus Diffuse Field, Near versus Far Field, Siemens, 2021. https://community.sw.siemens.com/s/article/sound-fields-free-versus-diffuse-field-near-versus-far-field (accessed Dec. 01).
[25] AZO Materials, "Aluminum Nitride (AlN) - Properties and Applications," 2001. https://www.azom.com/article.aspx?ArticleID=610 (accessed Dec. 01, 2021).
[26] M.W. Chase, NIST-JANAF Thermochemical Tables, 4th Edition, American Institute of Physics, 1998.
[27] DuPont Fluorochemicals, Thermodynamic Properties of HFC-134a, DuPont Fluorochemicals, 2004, p. 30. *Technical Information T-134a - SI.* Accessed: Dec. 23, 2021. [Online]Available: https://www.general-refrigeration.gr/images/eshop/catalog/products/0454/files/R134athermodynamic properties.pdf.
[28] B.N. Taylor, C.E. Kuyatt, Guidelines for Evaluating and Expressing the Uncertainty of NIST Measurement Results, National Institute of Standards and Technology, Gaithersburg, MD, 1994. *NIST Technical Note 1297.*